Post-Print of an Accepted Manuscript on the Laboratory of Turbulent Flows Website

Complete citation:

The final publication is available at https://doi.org/10.1016/j.expthermflusci.2021.110562

The Accepted Manuscript begins on the next page.

Large-scale 3D-PTV measurement of Ahmed-body wake in crossflow

Adriaan Booysen · Prashant Das · Sina Ghaemi[†]

Department of Mechanical Engineering, University of Alberta, Edmonton, Alberta T6G 2R3, Canada

[†] ghaemi@ualberta.ca

Abstract

The near wake of the Ahmed body at zero-yaw has been extensively studied in the literature, but comparatively little is known about the wake flow in crossflow condition. In this investigation, we characterize the near wake of a square-back Ahmed body at a Reynolds number of $Re_H = 9.2 \times 10^4$ for three yaw angles of $\beta = 0°$, $5°$, and $10°$. The measurements are carried out using 3D particle tracking velocimetry utilizing an innovative helium-filled soap bubble (HFSB) system for seeding a large domain of approximately $35 \times 30 \times 18$ cm^3. The results showed that increasing the yaw angle shifted the separation bubble towards the windward side and enlarged the recirculating region of the leeward side. The downwash motion from the top-edge and the spanwise motion from the leeward edge of rear-face also strengthened. A vortex ring formed in the periphery of the mean separation bubble. With increasing the yaw, the ring skewed toward the leeward edge and its windward potion became weaker. For the yaw cases, streamwise vortices appeared originating from the windward portion of the vortex ring. Spectral analysis showed that the overall energy of oscillations increased with yaw while the Strouhal numbers of the spanwise and wall-normal flow motions remained relatively constant. Proper orthogonal decomposition of the velocity field showed that the first spatial mode contained 32.8% of the total kinetic energy for the zero-yaw case. The energy of the first spatial mode reduced to approximately 10% for the $\beta = 5°$ and $10°$ wakes due to the disappearance of the bi-stability mode. The energetic flow motions within the yawed wakes were primarily on the windward side of the body.

1   Introduction

The aerodynamic performance of most vehicles has a large influence on their overall ability to meet the efficiency and safety requirements. Large vehicles such as transport trucks, buses, and delivery vehicles are generally bluff bodies that share the aerodynamic characteristics of having large, highly three-dimensional flow separation regions that generate a large pressure drag. In addition to the pressure drag, crosswinds can be detrimental to the handling, stability, and efficiency of vehicles that resemble a bluff body. In real world scenarios, driving rarely occurs without any form of crossflow (SAE International 2012; Dalessio et al. 2017). A clear

1

understanding of flow structures that develop in the wake flows of bluff bodies under cross-wind conditions is therefore critical to improving their aerodynamic performance.

For the study of automotive bluff bodies, a simplified research model that retains only the fundamental features was introduced by Ahmed et al. (1984) (henceforth referred to as the 'Ahmed body'). These features included a large frontal area to displace the flow, a long mid-section to allow any separated flow to reattach, and bluff afterbody which creates a large wake. The body sits on four posts lifting it off the ground to approximate the influence of the tires and the vehicle's proximity to the roadway. Different vehicle configurations can be represented by changing the angle of the rear slope of the body. The square-back Ahmed body is an iteration of the Ahmed body that has no slope in the rear section (Ahmed et al. 1984), leading to a flat rear face. The aspect ratio of this body does differ from transport vehicles but it has been shown that fundamental flow features remain the same (Grandemange et al. 2013a).

The flow past a square-back Ahmed body at zero yaw angle has been extensively investigated in the literature. Through experimental analysis, Khalighi et al. (2001) found that the time-averaged wake consisted of a large separation bubble that was symmetric across the spanwise plane, and slightly asymmetric across the wall-normal plane due to ground effects. At a height-based Reynolds number of $Re_H = 1.7 \times 10^5$, they also identified a large torus shaped vortex structure within the near wake of the mean flow field. Pressure measurements on the rear face demonstrated a frequency peak at a height based Strouhal Number of $St_H \sim 0.07$. This frequency was hypothesized to be a bubble pumping mode where the stagnation point of the recirculation bubble periodically shifted along the streamwise axis. The pumping mechanism was later attributed to pressure fluctuations caused by the stretching and squeezing of the vortices (Volpe et al. 2015; Pavia et al. 2018).

The investigation of Grandemange et al. (2013b) measured velocity, force, and pressure to characterize the wake of a zero-yaw square-back Ahmed body at $Re_H = 9.2 \times 10^4$. The most notable observation was the presence of a symmetry breaking, bi-stability phenomenon that imposed asymmetric recirculation zones along the spanwise dimensions within the instantaneous flow field. The bi-stability phenomenon consisted of two equiprobable states that imposed an asymmetric recirculation structure along the spanwise dimension of the near wake. The two states of the bi-stability mode switched randomly with a time scale three orders of magnitudes larger than H/U_∞. Since the switching was determined to be random, there was no distinct frequency associated with it. Lastly, two dominant frequency modes were identified corresponding to $St_H = 0.127$ and 0.174. The first mode was determined to stem from spanwise oscillations of the wake and the second from wall-normal oscillations of the wake, both caused by vortex shedding. A subsequent study by Volpe et al. (2015), confirmed the two shedding modes found by Grandemange et al. (2013b). They also observed a third frequency peak at $St_H = 0.08$, which is the bubble pumping mode, introduced earlier in the studies of Khalighi et al. (2001; 2012). Most recently, multiple studies (Pavia et al. 2018; 2020; Fan et al. 2020) have identified the energetic turbulent structures within the zero-yaw wake using proper orthogonal decomposition (POD). Pavia et al. (2018) characterized spatial POD modes using experimental measurements of base pressure and 2D

2

particle image velocimetry (2D-PIV) within the wake of a Windsor model at $Re_H = 7.7 \times 10^5$. They attributed the first mode to the spanwise symmetry breaking of the wake, finding that the temporal characteristics were closely related to those of the bi-stability phenomenon. Subsequent modes were attributed to vertical symmetry breaking and symmetry preserving mechanisms.

Several attempts have been made to characterize the topology of vortical structures within the wake at zero yaw angle, using various 2D velocity measurements. It was proposed by Duell and George (1999), that the vortex structures within the time-averaged flow field consisted of a single toric vortex and this interpretation was reaffirmed by several studies (Khalighi et al. 2001; Khalighi et al. 2012; Krajnović and Davidson 2003; Rouméas et al. 2009). Grandemange et al. (2013b) argued that the toric flow topology is not representative of the instantaneous wake organization due to the bi-stability phenomenon. Using a simulation based on lattice-Boltzmann method (LBM) at $Re_H = 3.96 \times 10^5$, Lucas et al. (2017) identified a skewed torus with one lateral side skewed upstream towards the rear face of the Ahmed body. This structure was identified from a flow field averaged over one bi-stability period, providing insight into the quasi-instantaneous structure of the vortex. Further support for this description came from large eddy simulation (LES) of a square-back Ahmed body at $Re_H = 3.3 \times 10^4$ by Dalla Longa et al. (2019). The instantaneous contours of pressure indicated the core of a phase-dependent, tilted, toroidal structure. Large hairpin vortices were shed from the downstream tilted side of the toroidal structure. It was suggested that a large enough hairpin vortex being shed could destabilize the toroidal structure and cause the switching between the bi-stability modes. Other studies on various square-back bodies (Evrard et al. 2016; Perry et al. 2016; Pavia et al. 2018; 2020; Fan et al. 2020), have also suggested that the instantaneous wake consists of hairpin-like vortices that are positioned along one side of the rear face with legs that traverse across the wake to the opposite spanwise side.

In contrast to the abundant investigations of the zero-yaw cases, there are only a few investigations of the wake of different vehicular bluff bodies in crossflow. Howell (2015) studied the drag on a variety of automotive shapes at yaw angles (β) smaller than 25°, and found that the drag increased almost linearly with yaw angle. The additional drag was described as an "induced" drag component, which was proportional to the sum of the squares of the lift and side forces. Volpe et al. (2014) investigated the effects of unsteady crossflow (transient gusts) over a square-backed Windsor body using a double wind tunnel. They observed that the side force coefficient is approximately 7% larger in the case of transient wind guests relative to the steady crossflow condition. The lateral force was also observed to lag the wind gust. An analysis of the sensitivity of the bi-stability phenomenon with respect to β by Volpe et al. (2015) on the square-back Ahmed body showed that bi-stability was completely suppressed when $\beta > 1°$.

Using planar PIV, Li et al. (2019) observed that at $\beta = 5°$, the separation bubble was skewed and the Reynolds stresses were larger along the windward shear layer of a square-back Ahmed body. Another study by Lorite-Díez et al. (2020) carried out PIV measurements across the mid-height of a square-back Ahmed body wake at three yaw angles of $\beta = 0°$, 5°, and 10°. They noted that the yawed flow deflected the recirculation bubble towards the leeward side of the wake. A decrease in the recirculation bubble length was also measured as the yaw angle increased. Gohlke

et al. (2007) experimentally investigated a Willy model for β up to 30° at $Re_{L}= 2.2\times10^6$. Two primary counter rotating vortices formed along the leeward face of the body. These vortices separated from the body at $\beta > 10°$. A subsequent Lattice Boltzmann simulation by Gohlke et al. (2008), identified three more vortices within the wake. They found a vortex ring that formed along the edges on the rear face, and two more vortices that extended out from the rear face. However, these observations may not apply to an Ahmed body since the Willy model has rounded edges along the length of the body.

The previous investigations show the complex 3D nature of the turbulent wake that form behind idealized bluff bodies at zero yaw angle. The topologies of the wakes for crossflow cases is still unknown and is addressed in the present investigation using state-of-the-art three-dimensional particle tracking velocimetry (3D-PTV). The potential of volumetric flow measurements for identifying 3D structures is apparent, and has been recently realized by the tomographic PIV measurement of the wake of a Windsor body at zero-yaw by Pavia et al. (2020). Using the 3D-PTV technique, we investigate the wake of a square-back Ahmed body for $\beta = 0, 5,$ and 10° at $Re_{H} = 9.2\times10^4$. To measure the flow in the whole wake, we developed a system to generate helium-filled soap bubbles (HFSB) for 3D-PTV tracers. The resulting measurements allow for the characterization of the yawed wake up to $\beta = 10°$. The 3D mean flow is compared for all three cases to assess the effects of crossflow on near wake characteristics such as velocity distributions, vortex filaments, recirculating zones, and Reynolds stresses. Spectral properties are then analyzed to evaluate the impact of yaw on instantaneous wake dynamics. Finally, proper orthogonal decomposition is performed on each case, giving insight into the high energy motions within the wake.

2   Experimental setup

Flow measurements in the wake of the square-back Ahmed body were carried out in a closed-loop wind tunnel located at the University of Alberta. The test-section of the wind tunnel has a cross section of 2.4 m × 1.2 m and is located after a nozzle with a contraction ratio of 6.3:1. The details of the experimental setup, including flow seeding and 3D-PTV system are provided in the subsections below.

2.1   Ahmed body setup
The study investigated the flow past a half-scale square-back Ahmed body. The dimensions of the wind-tunnel model were 522 mm in length (L) × 195 mm in width (W) × 144 mm in height (H). Figure 1 shows a schematic of the experimental set up. The origin of the coordinate system was centred along the width and height of the Ahmed body's rear face at zero yaw as seen in the upper right inset of Figure 1. The coordinate system was fixed with respect to the wind tunnel with its x-axis aligned with the flow direction. The y-axis corresponds to the spanwise direction, the z-axis corresponds to the direction normal to the flat plate located under the Ahmed body (wall-normal direction). The yaw angle, β, is the angle between the Ahmed body and the x axis in the

xy-plane. For this experiment, three cases were analyzed, corresponding to yaw angles of $\beta = 0°$, 5°, and 10°, which span a range of realistic crossflow driving conditions (SAE International 2012; Dalessio et al. 2017). Henceforth, the side of the body angled upstream will be referred to as the windward side and the opposite will be referred to as the leeward side. All measurements were made at a freestream velocity of $U_\infty = 10$ m/s. This corresponds to a Reynolds number of $Re_H = 9.2 \times 10^4$ based on body height and free stream flow-speed which is close to that of multiple other studies (Ahmed et al. 1984; Grandemange et al. 2013b; 2001; Dalla Longa et al. 2019). The body was mounted on a rotary table with a yaw angle precision of $\beta = \pm 0.5°$. The zero-yaw alignment was verified using planar PIV measurements across the mid-height of the wake to confirm the existence of both bi-stable modes, based on the wake organization. At the largest yaw angle of $\beta = 10°$, the blockage of the Ahmed body relative to the cross-sectional area of the wind tunnel was 1.4%. As can also be seen in the Figure 1, the Ahmed body was positioned on a flat plate that was installed 110 mm above the wind tunnel floor. A similar configuration has been used by previous investigations (Gohlke et al. 2007; Grandemange et al. 2013b; Volpe et al. 2015). The plate raises the Ahmed body above the turbulent boundary layer that forms on the wind tunnel floor. The bottom face of the Ahmed body was 25 mm above the plate and the plate's leading edge was 200 mm ahead of the Ahmed body.

2.2   Helium-filled soap bubbles

Helium-filled soap bubbles (HFSB) were used as tracer particles for carrying out the 3D-PTV measurements. The HFSB tracers are neutrally buoyant and have a diameter of approximately 0.5 mm that is several orders of magnitude larger than the conventional ~1 µm droplets typically used for particle tracking velocimetry (Scarano et al. 2015). The greater scattered light by HFSB tracers makes it possible to carry out 3D-PTV in volumes that are orders of magnitude larger than those achieved by 1 µm fog droplets. The system used to generate the HFSB was developed in-house and is based on the design of Gibeau et al. (2018). The HFSB nozzles were 3D-printed orifice type nozzles which have been shown to be well suited for experimental PIV and PTV applications (Gibeau et al. 2018; 2020, Faleiros et al. 2018; 2019). In order to seed the large volume required for this study, the original system of Gibeau et al. (2018) was scaled up to accommodate 48 nozzles.

The scaled-up system consisted of four ducts with each duct carrying 12 HFSB nozzles as shown in in the upper-left inset of Figure 1. The nozzles pointed downward and were staggered horizontally to minimize the potential for coalescence of the bubbles. The ducts were supported by two vertical stands with NACA 0012 profiles to provide streamlined housing units for the tubing. Regulated flow rates of air, helium, and soap were distributed to each nozzle through three separate tubes. The stand was positioned upstream of the contraction nozzle in the settling chamber of the wind tunnel. Using hot-wire probes, Gibeau et al. (2020) measured the effect of a similar HFSB system on the test-section turbulent intensity. They observed that at a free stream velocity of $U_\infty = 10$ m/s, the turbulence intensity of the test section increased from 0.4% to 0.6% due to the presence of the HFSB system in the settling chamber.

Gibeau et al. (2020) also experimentally characterized the response time of HFSB tracers by measuring their deceleration near the stagnation point of an airfoil. The investigation found that the bubbles were on average neutrally buoyant while the standard deviation of the response time was 150 μs. The bubbles had a mean size of approximately 400 μm and were produced at an approximate rate of 50,000 bubbles per second per nozzle.
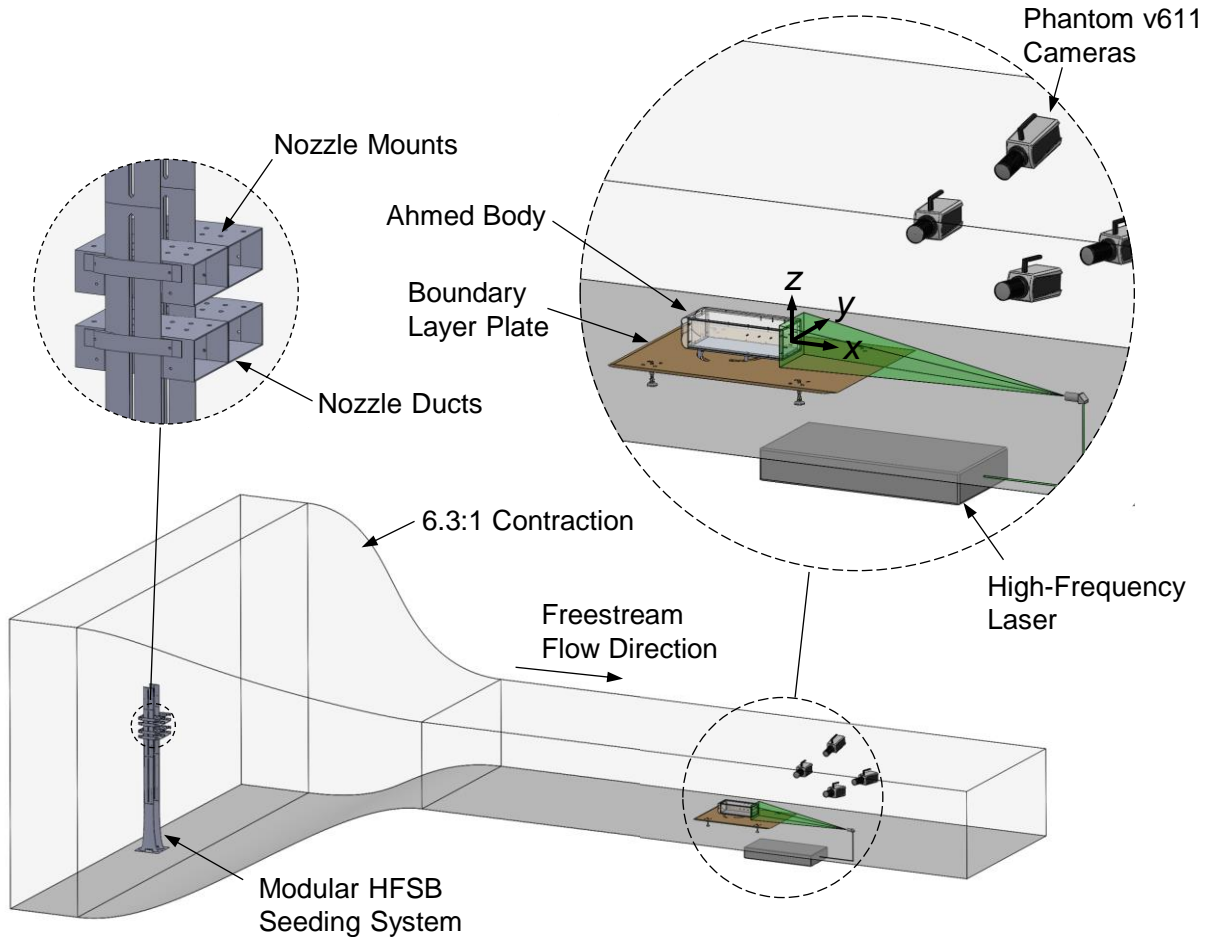

Figure 1: A schematic of the experimental setup showing the wind tunnel, Ahmed body, flat-plate, 3D-PTV system, and the nozzles used for generating the helium-filled soap bubbles.

2.3 Large-scale 3D particle tracking velocimetry

For 3D-PTV measurements, the wake of the Ahmed body was illuminated using a high-repetition dual-cavity Nd:YLF laser (Photonics Industries) with a pulse energy of 20 mJ per cavity. The laser beam was expanded using a spherical concave lens with a focal length of -100 mm. The expanded beam was cropped to the form a rectangular cross-section using knife-edges. The illuminated volume was imaged using four high-speed CMOS cameras (Phantom V611) with a sensor size of 1280×800 pixels, each pixel being 20×20 μm^2. The cameras were equipped with

SLR lenses with a focal length of $f = 105$ mm which were connected to the camera bodies using Scheimpflug adapters. The imaging distance of the lens was approximately 1.6 m, with the apertures set at $f/16$. The magnification of the cameras was approximately 0.067. The resulting images of the HFSB particles were Gaussian and approximately 2-3 pixels in diameter. A seeding density of 0.02 particle per pixel was obtained in the 3D-PTV images. The imaging system was calibrated using a dual-plane target with the planes separated by 3 mm. The target was placed parallel to the xz-plane on a traverse, and a total of three views, 5 mm apart, were recorded by traversing the target along the y-axis. These images were then used to obtain a mapping function for the measurement volume using a 3rd order polynomial fit in Davis 10.1 (LaVision GmbH).

The final measurement volume for the $\beta = 0°$ case was approximately 350 mm × 240 mm × 180 mm ($x \times y \times z$). For the $\beta = 5°$ and 10° cases, the measurement volume was approximately 350 mm × 300 mm × 180 mm ($x \times y \times z$) to cover a wider wake region. Figure 2 shows the size and position of the measurement volumes for each case as well as the rotation of the Ahmed body. The measurement volumes were located in the wake region of the Ahmed body, each with a slight overlap with the rear of the body. Note that the coordinate system is fixed with respect to the wind tunnel, therefore the x-axis remains parallel to the streamwise direction for all cases.
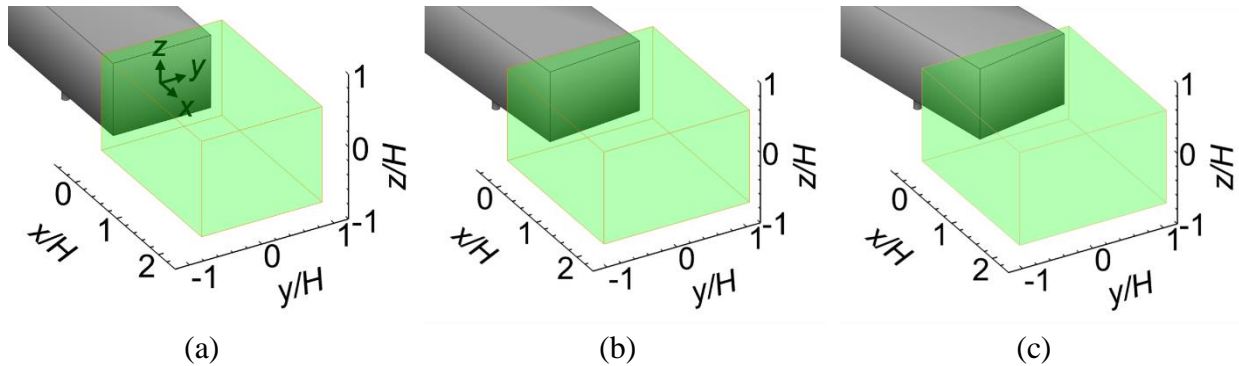

Figure 2: The illuminated measurement volumes in the wake flow of the Ahmed body for yaw angles of a) $\beta = 0°$, b) $\beta = 5°$, and c) $\beta = 10°$.

The recorded images were processed using a commercial software (Davis 10.1, LaVision Gmbh). First, the minimum intensity of the images ensemble was subtracted from each image to remove any background intensity. The images were then normalized using the ensemble average of the images. A volume self-calibration process was applied on the resulting images to eliminate the remaining calibration disparities (Wieneke 2008). An optical transfer function was also estimated (Schanz et al. 2013). Finally, the shake-the-box (STB) algorithm (Schanz et al. 2016) was applied to obtain Lagrangian particle tracks in the measurement volume. For each time instant, approximately 10,000 tracks were detected. Figure 3 shows a snapshot of the 3D particle tracks showing four successive time-steps at $\beta = 0°$. To visualize the core of the wake, only the half of

the measurement volume that occupies the positive *y* region is shown here. As it is observed, the freestream, the shear layer and the recirculating flow are captured in the measurement volume.

To improve the statistical convergence of time-resolved data, we used a cyclic procedure for data collection. For each yaw angle, we collected 4 sets of 250 cycles of images. The cycles were collected at 40 Hz, while 20 time-resolved images were recorded within each cycle at 2.5 kHz. At the latter frequency, the maximum particle displacement in the freestream region was roughly 10 pixels between successive images. The time-resolved images within each cycle were needed for the STB algorithm, while the low frequency cycles ensured convergence of turbulence statistics. A single concurrent frame from all 1000 cycles was used for calculating the statistics, resulting in a temporal resolution of 40 Hz. Overall, the total duration of measurement using this setting was 25 s spanning over 1000 cycles. This is equivalent to approximately $1700H/U_\infty$, which is longer than the time-scale of the bi-stabilities. To obtain the mean flow statistics, the velocity vectors of the particles obtained from the 1000 frames were combined into a single velocity field that was binned into small volumes with dimensions of 15×15×15 mm and 50% overlap. For obtaining the Eulerian instantaneous velocity fields, the velocity vectors of particles in each instantaneous field were binned into 30×30×30 mm cubes with 75% overlap. These time-resolved velocity fields were used for the proper orthogonal decomposition (POD) analysis.

A second data acquisition method was also implemented for spectral analysis of the wake. For each yaw angle, 4 time-resolved sets were collected at 2.5 kHz. Each set was 2.2 s, leading to a total duration of 8.8 s for each yaw angle. The processing of these sets was carried out in the same manner as the cyclic data, and the instantaneous particle fields were binned into 30×30×30 mm cubes with 75% overlap. When calculating the spectra, the individual spectrum for each set was calculated first and then all four spectra were averaged.

The estimated uncertainties of the 3D-PTV system were 0.1 pixels along the in-plane *x* and *z* axes, and 0.2 pixels for the out-of-plane *y*-axis (Ebrahimian et al. 2019; Rowin et al. 2019). Using the digital resolution of 0.294 mm/pixel and the imaging frequency of 2.5 kHz, the corresponding velocity uncertainties were $0.0074U_\infty$ along the *x* and *z* axes and $0.0148U_\infty$ along the *y*-axis. It should also be noted that for the following discussion, the time averaged velocity components will be denoted by $\langle U \rangle$ for the streamwise direction, $\langle V \rangle$ for the spanwise direction, and $\langle W \rangle$ for the wall-normal direction. The corresponding fluctuating velocity components will be denoted by *u*, *v*, and *w*.
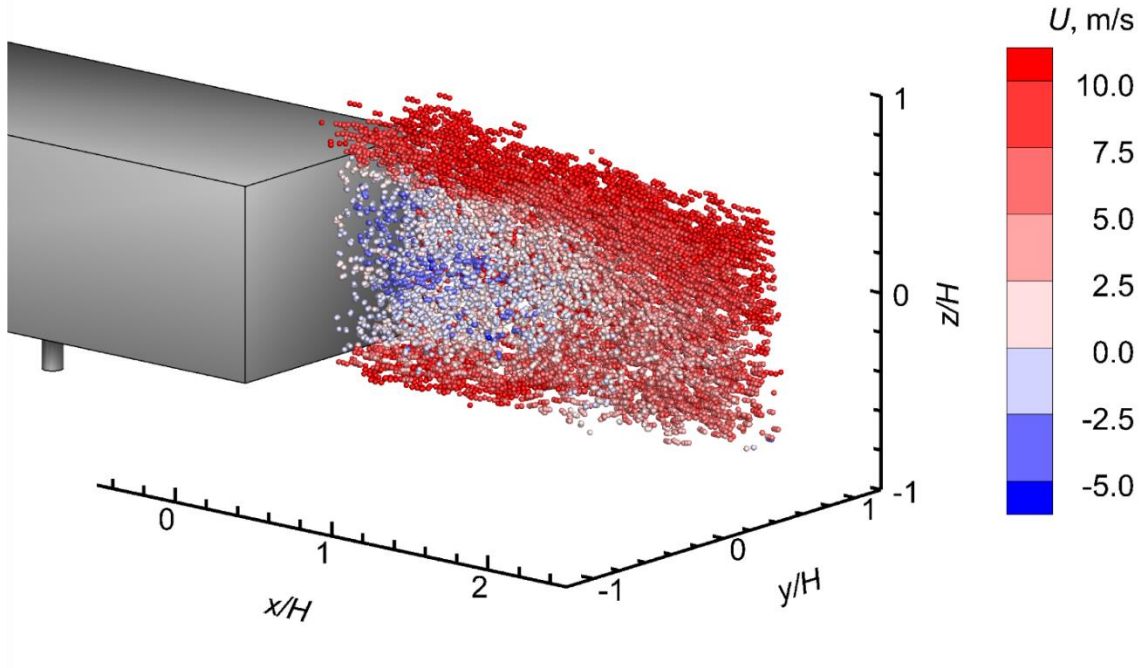
Figure 3: A visualization of Lagrangian velocities in four consecutive 3D-PTV time-steps. Only the $y/H > 0$ half of the velocity field is shown to visualize the low-speed core of the wake. A video showing the density of the instantaneous Lagrangian velocities for the full wake of the $\beta = 0°$ case is also provided within the supplementary material for this article.

3   Mean velocity fields

We start with investigating the mean flow field for all three yaw cases. The mean velocity field of the $\beta = 0°$ case acts as a reference for analyzing the effects of crossflow and is shown in Figure 4. In Figure 4(a), (b), and (c), 3D isosurfaces of $\langle U \rangle/U_\infty = 0$, $\langle V \rangle/U_\infty = \pm 0.1$, and $\langle W \rangle/U_\infty = \pm 0.1$ are shown, respectively. The red isosurfaces represent the positive velocity component and blue represent the negative. Figures 4(d) and (e) show in-plane streamlines and contours of $\langle U \rangle/U_\infty$ and $\langle V \rangle/U_\infty$ at $z/H = 0$ plane, respectively. Figure 4(f) shows in-plane streamlines and contours of $\langle W \rangle/U_\infty$ across the $y/H = 0$ plane. Here, we refer to the region enclosed by the $\langle U \rangle/U_\infty = 0$ isosurface in Figure 4(a) as the separation bubble. The separation bubble appears relatively symmetric and elongated in the streamwise direction. In the 2D slice of Figure 4(d), we see that the region of recirculating streamlines, named the recirculation bubble, extends to $x/H = 1.5$, which is consistent with the experimental observations of Grandemange et al. (2013b) made at $Re_H = 9.2 \times 10^4$. To make the difference between the separation bubble and recirculation bubble clear, a green line representing the separation bubble in Figure 4(a) has been overlayed onto Figure 4(d), (f). The separation bubble passes through the focal points of the two in plane recirculating vortices whereas the recirculation bubble is formed by the encircling streamlines. It is also worth noting that the

9

streamwise lengths of the separation bubble and recirculation bubble match. The streamlines also show a slight asymmetry between the two recirculation regions, which is attributed to the imbalance of one of the bi-stable states in the mean flow field (Volpe et al. 2015).

The isosurfaces of $\langle V \rangle/U_\infty = \pm 0.1$ in Figure 4(b) are relatively equal in size and positioned symmetrically. The exception is a small isosurface of $\langle V \rangle/U_\infty = -0.1$ close to the base of the Ahmed body, for which a positive counterpart is not visible. Inspection of $\langle V \rangle$ contours in Figure 4(e) shows that a region of positive $\langle V \rangle$ also exists close to the base at $y/H > 0$ but it is relatively weaker. In general, Figure 4(e) demonstrates a relative symmetry of the spanwise mean flow with respect to $y/H = 0$ plane. The isosurfaces indicate that zones of large $\langle V \rangle$ are located downstream of the rear-face at approximately $x/H = 1.2$ where the streamlines curve around the separation bubble.

The isosurfaces of $\langle W \rangle/U_\infty = \pm 0.1$ in Figure 4(c) and contours of Figure 4(f) show a large zone of downward motion from the top edge of the Ahmed body and a smaller zone of upward motion on the bottom edge. This asymmetry is due the ground plane limiting the flow underneath the Ahmed body. As discussed by Rouméas et al. (2009) and Grandemange et al. (2013b; 2015), the increased flow from overtop of the body compensates for the restricted flow from underneath. Streamlines in Figure 4(f) show the maximums of wall-normal velocity are located outside of the recirculation bubble where the streamlines curvature is large. We also see two large recirculation zones in the wall-normal cross-section of the separation bubble.

The volumetric data obtained for the wake in this study also allowed for the identification of 3D vortex structures within the mean flow. Vortex filaments are identified using the critical-point theory described by Sujudi and Haimes (1995). This method has been effectively used in similar bluff body studies (Östh et al. 2012; Zhu et al. 2017). The vortex centers that are shown in the current investigation were also confirmed by visual inspection of the 3D streamlines. The 3D streamlines are omitted here for clarity of the figures. The resulting vortex center for the zero-yaw case is shown by the thick red line in Figure 4(a). The vortex filament indicates the presence of a ring vortex (RV) that lies on the $\langle U \rangle/U_\infty = 0$ isosurface. The ring is centered at approximately $x/H = 0.71$ and is shifted slightly downstream at the midspan. This vortex structure is consistent with the toric structure reported for time-averaged wakes in previous studies (Khalighi et al. 2001; 2012; Krajnović and Davidson 2003; Rouméas et al. 2009; Perry et al. 2016).
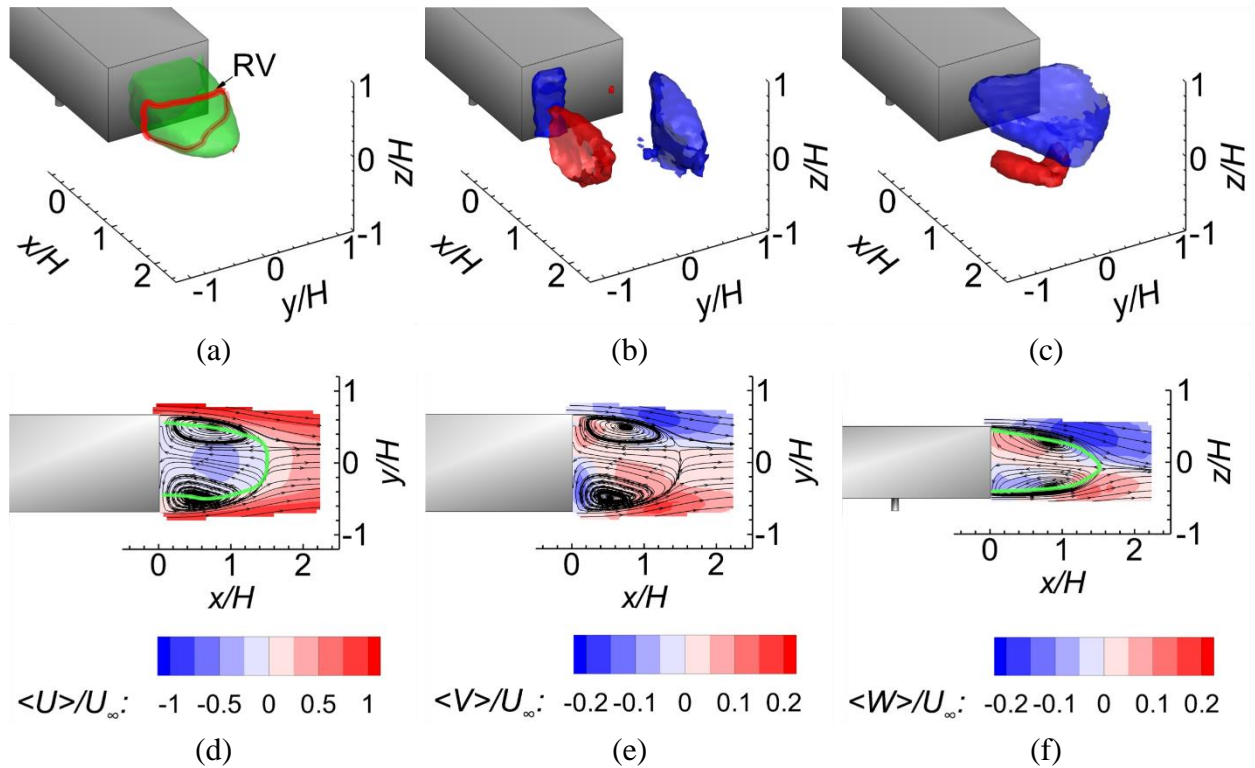
Figure 4: Visualization of the mean velocity components for the $\beta = 0°$ case. (a) The green isosurface shows $\langle U \rangle /U_\infty = 0$, (b) the red isosurface corresponds to $\langle V \rangle /U_\infty = 0.1$ and the blue indicates $\langle V \rangle /U_\infty = -0.1$. (c) The red isosurfaces corresponds to $\langle W \rangle /U_\infty = 0.1$ and blue to $\langle W \rangle /U_\infty = -0.1$. The slices show (d) contours of $\langle U \rangle /U_\infty$ at the $z/H = 0$ plane, (e) $\langle V \rangle /U_\infty$ contours at the $z/H = 0$ plane, and (f) $\langle W \rangle /U_\infty$ contour at the $y/H = 0$ plane. The red line seen in (a) represents the ring vortex (RV) identified within the mean flow field. The green line in (d,f) shows the perimeter of the separation bubble indicated by $\langle U \rangle /U_\infty = 0$.

The effects of yaw on the time-averaged flow field for $\beta = 5°$ is shown in Figure 5. The presentation of the results in Figure 5 is consistent with Figure 4. The $\langle U \rangle /U_\infty = 0$ isosurface in figure 5(a) is asymmetric with respect to $y/H = 0$ plane, with the bulk of this separation bubble being positioned on the windward side of the wake. This separation bubble has a streamwise length of $x/H = 1.5$ which remains similar to the zero-yaw case. The separation bubble position is again represented by the green lines in Figure 5(d), (f). The vortex filament shown in Figure 5(a) also forms a skewed RV. The leeward side of the RV filament is closer to the Ahmed body relative to the windward side of the filament. This ring vortex is similar to the skewed torus that was previously identified for a single symmetry-breaking mode of the zero-yaw case (Lucas et al. 2017; Dalla Longa et al. 2019). This commonality could suggest that the yawed vortex ring structure is a progression of the skewed instantaneous torus of the zero-yaw case. In addition to the main

vortex ring, two streamwise vortex cores, identified as SV1 and SV2 in Figure 5(a), are also noted on the windward side of the body. These vortices extend downstream starting from the RV.

The velocity distributions in Figure 5(b) and (e) show a large increase in positive spanwise flow from the leeward side of the wake. Two smaller zones of negative spanwise velocity are also identified, one located along the rear face and one downstream along the windward side of the wake. The negative zone on the rear face is larger than the negative zone observed in the zero-yaw wake. The 3D isosurface in Figure 5(b) shows that the positive spanwise velocity on the leeward side is stronger along the mid-height of the wake. The two regions of negative spanwise velocity extend primarily in the z direction. Streamlines across the spanwise xy-plane in Figure 5(d) show a large recirculating vortex forming on the leeward side of the rear face, while a smaller recirculating vortex is seen further downstream on the windward side.

The isosurfaces of $\langle W \rangle$ in figure 5(c) show that both the zones of positive and negative velocity have become larger relative to the zero-yaw case. The primary region of negative wall-normal velocity is now asymmetric with respect to $y/H = 0$ plane, being larger on the leeward side. The magnitude of the wall-normal velocity component is also significantly stronger as seen by comparing Figure 5(f) with 4(f). The positive $\langle W \rangle$ isosurface is still smaller than the negative $\langle W \rangle$ component and is predominantly distributed on the lower half of the wake, close to the end of the recirculation bubble. Streamlines in Figure 5(f), which are on a plane located at the midspan of the rear face, show two recirculation regions along the top and bottom, with the top recirculation being smaller and shifted slightly downstream in comparison.
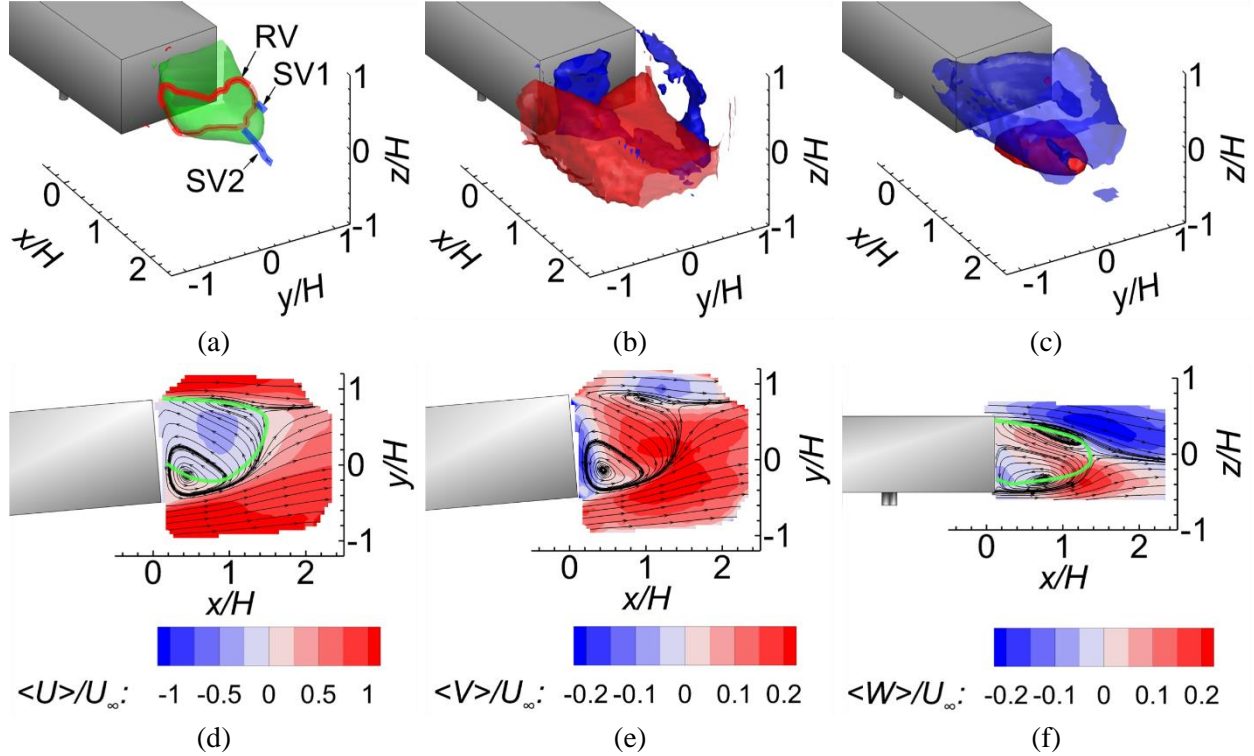
Figure 5: Visualization of the mean velocity components for the $\beta = 5°$ case. (a) The green isosurface shows $\langle U \rangle / U_\infty = 0$, (b) the red isosurface corresponds to $\langle V \rangle / U_\infty = 0.1$ and the blue indicates $\langle V \rangle / U_\infty = -0.1$. (c) The red isosurfaces corresponds to $\langle W \rangle / U_\infty = 0.1$ and blue to $\langle W \rangle / U_\infty = -0.1$. The slices show (d) contours of $\langle U \rangle / U_\infty$ at the $z/H = 0$ plane, (e) $\langle V \rangle / U_\infty$ contours at the $z/H = 0$ plane, and (f) the $\langle W \rangle / U_\infty$ contours at the $y/H = 0.184$ plane. The red and blue lines seen in (a) represent the ring vortex (RV) and streamwise vortex (SV) filaments, respectively. The green line in (d,f) shows the perimeter of the separation bubble indicated by $\langle U \rangle / U_\infty = 0$.

The isosurface of $\langle U \rangle / U_\infty = 0$ for $\beta = 10°$ in Figure 6(a) is also asymmetric across the span of the wake and favours the windward region. The size of the separation bubble is this time smaller, evident in a 7% smaller spanwise width relative to the $\beta = 5°$ case, as well as in a reduced separation bubble length of $x/H = 1.4$. The flow patterns inferred by the isosurfaces and in-plane velocity plots in Figure 6 remain consistent with the descriptions of the $\beta = 5°$ flow patterns discussed before. However, effects of increasing yaw are evident in the larger velocity magnitudes for both the spanwise and wall-normal velocity components. Figure 6(a) shows that the RV stretches in the wall-normal direction on the leeward side and then bends along the top and bottom of the separation bubble toward the windward side. The identified filament does not close on the windward side, suggesting that the strength of the vortex filament decreases below the threshold used for vortex identification. However, a weak vortex does exist on the windward side as can be verified by the streamlines in Figure 6(d). The streamwise filaments (SV1 and SV2) identified in

the $\beta = 5°$ case are also present and slightly longer. There are also two new vortex filaments, one at the top-windward corner (SV3) and one on the leeward side of the separation bubble (SV4).

The comparison between the three cases of $\beta = 0°$, $5°$, and $10°$ showed a large increase in the strength of positive spanwise and negative wall-normal motions as yaw angle increased. Increasing the yaw angle also resulted in a shorter recirculation bubble, and a larger leeward recirculating vortex. The observed asymmetry increases as well as the decreasing separation bubble length are both consistent with the findings of Lorite-Díez et al. (2020). The current study, however, measured the length of the 3D separation bubble instead of the 2D recirculating bubble, which may account for any disparities in exact length and trends with yaw. For the yawed cases, the maximum length of the separation bubble did not coincide with the mid-height plane. 3D vortex filaments revealed a single vortex ring that became progressively skewed as the yaw angle increased. In addition, streamwise vortex filaments appeared at $\beta = 5°$ and $10°$ and their length increased with the yaw angle.
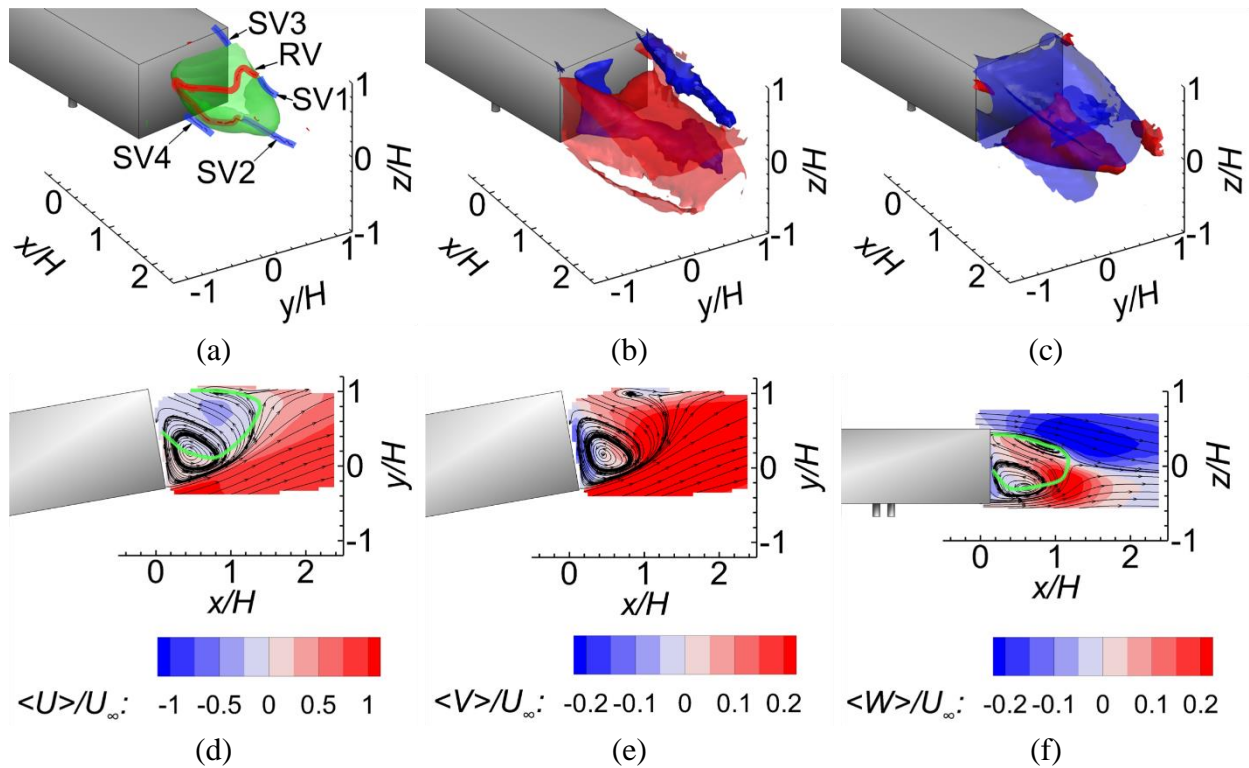

Figure 6: Visualization of the mean velocity components for the $\beta = 10°$ case. (a) The green isosurface shows $\langle U \rangle / U_\infty = 0$, (b) the red isosurface corresponds to $\langle V \rangle / U_\infty = 0.1$ and the blue indicates $\langle V \rangle / U_\infty = -0.1$. (c) The red isosurfaces corresponds to $\langle W \rangle / U_\infty = 0.1$ and blue to $\langle W \rangle / U_\infty = -0.1$. The slices show (d) contours of $\langle U \rangle / U_\infty$ at the $z/H = 0$ plane, (e) $\langle V \rangle / U_\infty$ contours at the $z/H = 0$ plane, and (f) $\langle W \rangle / U_\infty$ contours at the $y/H = 0.366$ plane. The red and blue lines seen in

14

(a) represent the ring vortex (RV) and streamwise vortex (SV) filaments, respectively. The green line in (d,f) shows the perimeter of the separation bubble indicated by $\langle U \rangle / U_\infty = 0$.

4   Reynolds stresses

Isosurfaces of the streamwise Reynolds stress for $\langle u^2 \rangle / U_\infty^2 = 0.05$ are shown in Figure 7. Across all three cases, the locations of the isosurfaces are consistent with shear layers forming along the perimeter of the rear face. The isosurface of the zero-yaw case is approximately symmetric with respect to the $y/H=0$ and $z/H=0$ planes, with the isosurface slowly contracting inwards toward the centerline with increasing x. The effects of yaw can be assessed in Figure 7(b) and (c), where the isosurface of $\langle u^2 \rangle$ along the leeward side of the body becomes smaller, and $\langle u^2 \rangle$ along the upper, lower, and windward sides increase in size. This observation is consistent with stronger shear layers on the windward side of the wake.
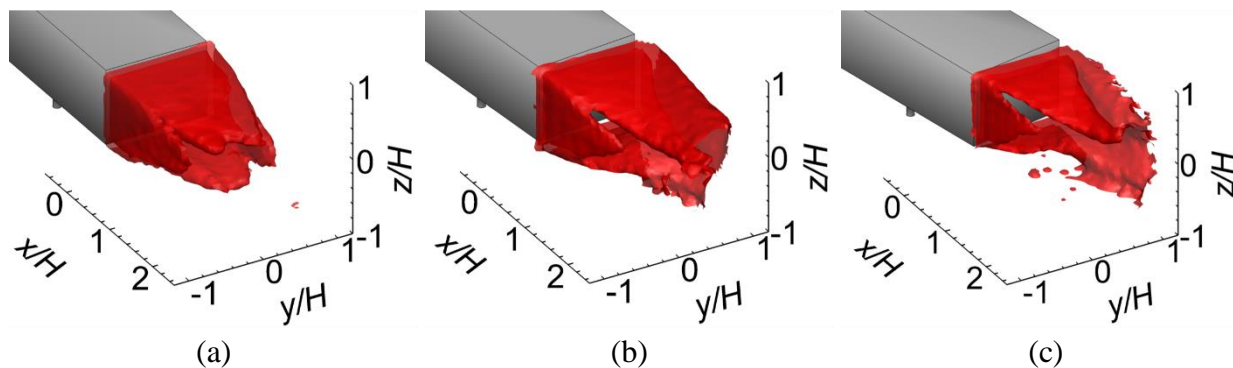

Figure 7: Isosurfaces of streamwise Reynolds stress at $\langle u^2 \rangle / U_\infty^2 = 0.05$ for yaw angles of (a) $\beta = 0°$, (b) $\beta = 5°$, and (c) $\beta = 10°$.

Isosurfaces of two Reynolds shear stresses are investigated in Figure 8; the three plots in the top row correspond to $\langle uv \rangle / U_\infty^2$ while the three on the bottom row correspond to $\langle uw \rangle / U_\infty^2$. The red isosurfaces show positive while blue isosurfaces show negative values. The isosurfaces of $\langle uv \rangle$ for the zero-yaw case are predominantly distributed along the spanwise limits of the recirculation bubble, tapering slightly as they extend downstream. The negative and positive distributions are symmetric and both isosurfaces have small inward bulges centered at the mid-height of the wake. The $\langle uv \rangle$ isosurfaces for $\beta = 5°$ in Figure 8(b) are asymmetric; the leeward isosurface is smaller and has a wall-normal tapering while the windward isosurface is larger and expands slightly in the wall-normal direction. Two smaller streamwise-elongated isosurfaces of positive and negative $\langle uv \rangle$ also extend downstream from the top windward edge, and one positive $\langle uv \rangle$ isosurface extends from the bottom windward edge. These isosurfaces can be visually identified as those falling between the two primary isosurfaces at the spans of the wake. The locations of these isosurfaces are consistent with the SV1 and SV2 vortices shown in Figure 5(a).

15

Figure 8(c) shows that the increase in yaw angle to $\beta = 10°$, increases the tapering of the positive $\langle uv \rangle$ distribution along the leeward side. No tapering is observed for the negative $\langle uv \rangle$ isosurface. The small streamwise elongated isosurfaces extending along the top and bottom of the wake are again present and slightly larger in size compared to the $\beta = 5°$ case. These $\langle uv \rangle$ extensions align well with the vortices identified in Figure 6(a), further supporting the proposed vortex topology.

Figures 8(d)-(f) show $\langle uw \rangle$ isosurfaces for each yaw case, all of them extending downstream from the top and bottom edges of the rear face. For the zero-yaw case, the negative $\langle uw \rangle$ isosurface is distributed over a larger area and has a greater peak magnitude relative to the positive isosurface. When the yaw angle increases to $\beta = 5°$, the $\langle uw \rangle$ distributions become asymmetric, also along the span of the wake. The wall-normal extent of the isosurfaces is greater on the windward side of the wake. The leeward sides of the $\langle uw \rangle$ isosurfaces also taper inwards towards the center. With the increase to $\beta = 10°$, a positive isosurface extends downstream from the top of the leeward edge. This formation is consistent with the SV4 vortex first observed in Figure 6(a) and supports the existence of a vortex extending downstream from the top leeward corner. Aside from this noted difference, the $\langle uw \rangle$ distributions for $\beta = 10°$ remain similar to those described for $\beta = 5°$.

The results show that with increasing the yaw angle, Reynolds shear stresses become stronger on the windward side. In contrast, on the leeward side, the Reynolds shear stresses become weaker and concentrated along the mid-height of the wake. The small streamwise-elongated zones of Reynold shear stress on the corners of the windward side indicate formation of streamwise vortices.
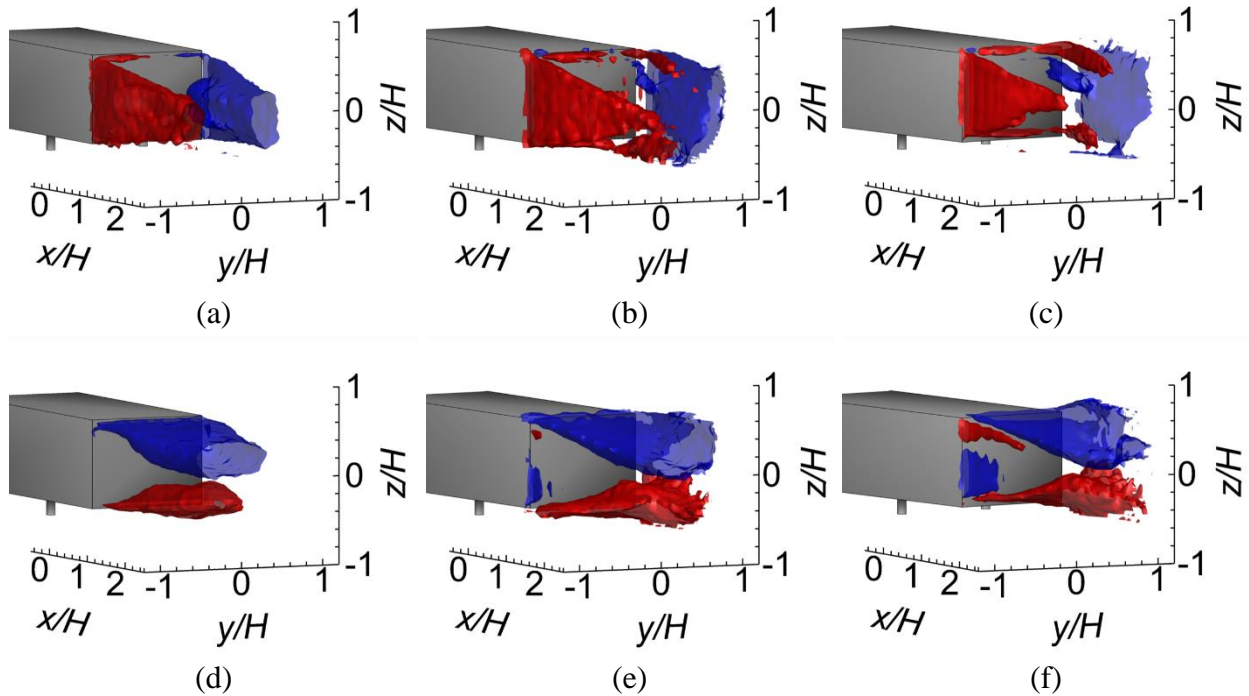

(a) (b) (c)

(d) (e) (f)

Figure 8: Isosurfaces of streamwise-spanwise Reynolds stress $\langle uv \rangle/U_\infty^2 = +0.01$ (red) and $\langle uv \rangle/U_\infty^2 = -0.01$ (blue) for the yaw angles of (a) $\beta = 0°$, (b) $\beta = 5°$, and (c) $\beta = 10°$. The streamwise-wall-normal Reynolds stress is visualized using isosurfaces of $\langle uw \rangle/U_\infty^2 = +0.01$ (red) and $\langle uw \rangle/U_\infty^2 = -0.01$ (blue) for (d) $\beta = 0°$, (e) $\beta = 5°$, and (f) $\beta = 10°$.

5 Spectral analysis of wake dynamics

To characterize the frequency of the wake dynamics during crossflow and how these differ from the zero-yaw case, the frequency-multiplied spectral densities (PSD) of the u-velocity component are evaluated. PSD was calculated using the time-resolved velocity fields measured at 2.5 kHz with a frequency resolution of $St_H = 0.0072$. For all the β angles, the PSD is locally averaged on a $3 \times 3 \times 3$ grid of neighboring data points centered at $(x, z) = (1.30H, 0.25H)$. The y location for $\beta = 0, 5, 10°$ cases is set to 0.45, 0.75, and 0.90H, respectively. The y locations were determined by calculating PSD spectra at various y locations across the wake and then choosing the locations with the highest peak intensity. These y locations coincided with the windward shear layers for the yawed cases. The resultant frequency-multiplied PSD ($St_H \times$ PSD) are shown in Figure 9.

The zero-yaw case is analyzed first and compared to previous investigations. Figure 9(a) shows the frequency-multiplied PSD spectrum from the probe at $(x, y, z) = (1.30H, 0.45H, 0.25H)$. Three peaks are identified at $St_H = 0.09$, 0.12, and 0.18. Based on the previous studies of Grandemange et al. 2013b and Volpe et al. 2015 on a square back Ahmed body geometry, these frequencies were attributed to side to side (spanwise) and ground-plane to top face (wall-normal) oscillations of the wake. The higher frequency peak at $St_H = 0.18$ is attributed to the wall-normal vortex shedding mode while the middle peak at $St_H = 0.12$ is attributed to the spanwise vortex shedding mode. The third peak at $St_H = 0.09$ closely matches the bubble pumping frequency previously identified by Khalighi et al. (2001; 2012) and Volpe et al. (2015). Out of the three peaks, the wall-normal shedding peak has the highest energy, followed by an even peak energy for the two lower frequency peaks.

Figure 9(b) shows the PSD spectrum for the $\beta = 5°$ case at $(x, y, z) = (1.30H, 0.75H, 0.25H)$; a point in the windward shear layer. Two peaks are identified at $St_H = 0.14$ and 0.19 which are both close to the two vortex-shedding peaks identified in the zero-yaw case. The low-frequency bubble-pumping that was observed for the zero-yaw case disappears. Since there are no fundamental changes in the mean flow characteristics summarized in Section 3, the lower peak at $St_H = 0.14$ is again attributed to spanwise shedding and the higher peak at $St_H = 0.19$ is attributed to wall-normal shedding. In general, the energy of the peaks shows a significant increase relative to the zero-yaw case as seen from the area under the frequency-multiplied PSDs. This indicates stronger wall-normal and spanwise vortex sheddings on the windward side of the $\beta = 5°$ case. The greater peak of the wall-normal shedding indicates that this motion is still more energetic relative to the spanwise vortex shedding at $(x, y, z) = (1.30H, 0.75H, 0.25H)$ location. Although not shown in

17

Figure 9, the turbulence energy of the spectrum on the leeward side was found to be insignificant relative to the windward spectrum.

The spectrum for $\beta = 10°$ is shown in Figure 9(c) where the probe point is again positioned in the windward shear layer at $(x, y, z) = (1.30H, 0.90H, 0.25H)$. Two peaks are identified at $St_H = 0.14$ and 0.17. The lower frequency peak remains the same as the $\beta = 5°$ case, but the high frequency peak reduces slightly to $St_H = 0.17$. These peaks are again attributed to spanwise and wall-normal shedding modes within the wake, respectively. The magnitude of the lower frequency peak is this time larger than that of the high frequency peak, indicating that the spanwise shedding is stronger that the wall-normal shedding. In addition, the energy within the total spectrum is significantly higher than the previous two cases, having both more energy contained within the spectrum as well as a peak energy that is almost three times greater than the previous maximum. Once again, the spectral energy on the leeward was also much less than the energy content on the windward side.

The spectra in Figure 9 make it possible to identify three different patterns within the wake oscillations as the yaw angle increases. When comparing the dominant frequencies identified for each case, two primary peaks are always present and the respective frequencies match closely for each peak ($St_H = 0.12$-0.14 and $St_H = 0.17$-0.19). This pattern suggests that an increase in yaw angle had negligible effect on the shedding St_H within the range of $0 \leq \beta \leq 10°$. The only variation between the spectra is therefore related to the energy content of the peaks at these characteristic frequencies. The second trend can then be seen when comparing the total energy content for each case. Increasing the yaw angle, significantly increases the energy contained within the spectrum, with the largest increase being between the two yawed cases. This is consistent with the larger $\langle u^2 \rangle$ isosurface observed in Figure 7 on the windward sides of the wake for $\beta = 5°$ and $10°$. The last trend is identified by comparing the energy of the two shedding mode peaks for each case. As the yaw angle increases, so does the comparative energy of the spanwise shedding peak with respect to the higher wall-normal frequency peak, eventually surpassing it in energy content for the $\beta = 10°$ case.
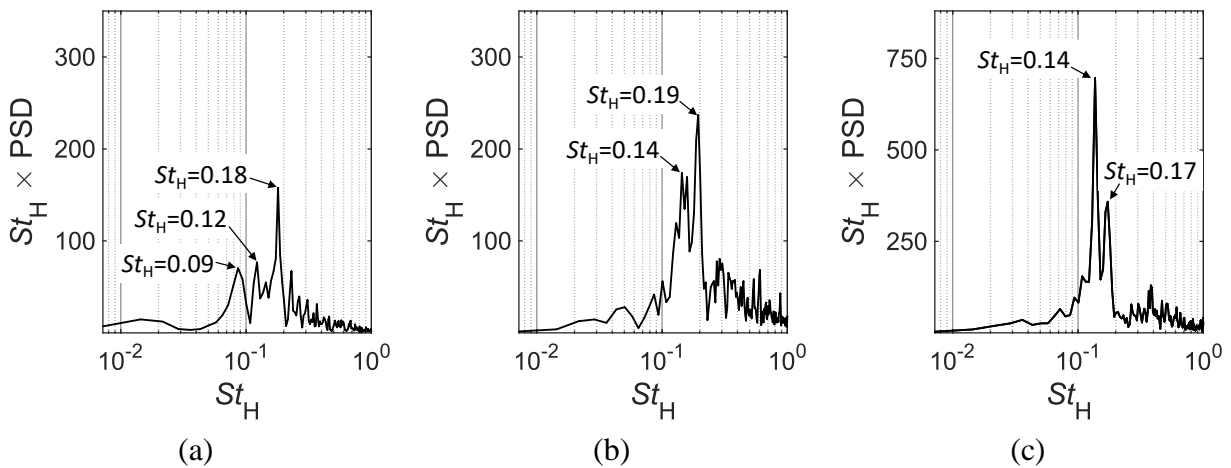

(a)   (b)   (c)

Figure 9: Frequency-multiplied PSD of streamwise velocity for yaw angles of $\beta = 0°$ (a), $\beta = 5°$ (b), $\beta = 10°$ (c). The PSD spectrum for the $\beta = 0°$ case is based on fluctuations at the coordinates of $(x, y, z) = (1.30H, 0.45H, 0.25H)$. The PSD spectrum for the $\beta = 5°$ case is based on fluctuations at the coordinates of $(x, y, z) = (1.30H, 0.75H, 0.25H)$. Lastly, the PSD spectrum for the $\beta = 10°$ case is based on fluctuations at the coordinates of $(x, y, z) = (1.30H, 0.90H, 0.25H)$.

6 Coherent motions using Proper Orthogonal Decomposition

Proper orthogonal decomposition (POD) is applied here based on the method of snapshots POD (Sirovich 1987) to identify the energetic motions. This study results in complete spatial modes since the POD algorithm is applied to a 3D velocity field, accounting for all three velocity components within a volume. However, for brevity, the following visualizations of the spatial modes only show the resulting u-components of the POD analysis. The data used for this analysis was the cyclic data with a temporal resolution of 40 Hz because it was collected over a large time span, improving the convergence of spatial modes.

The energy of the first 20 spatial modes as a percentage of the total turbulent kinetic energy of each case is presented in Figure 10. The energy distribution for the zero-yaw case (black) shows that the first mode contains 33% of the total energy while the first four modes for the zero-yaw case contain 44% of the total energy. In contrast to this, for the $\beta = 5°$ case (blue), mode one contributes to 9% of the total kinetic energy, and the first four modes contain 24% of the total energy. The yaw case of $\beta = 10°$ (red) has an energy content distribution similar to the $\beta = 5°$ case. For $\beta = 10°$, the first mode contribution is 11%, and the first four modes contain 28% of the total energy. The high energy content of the first mode for the zero-yaw case is the most apparent difference between the three cases. The higher energy of the first mode has been previously observed by multiple studies (Östh et al. 2014; Perry et al. 2016; Pavia et al. 2018; 2020; Fan et al. 2020), however, the energy content observed within this analysis is much higher still, underscoring the significance of 3D data used for the decomposition.
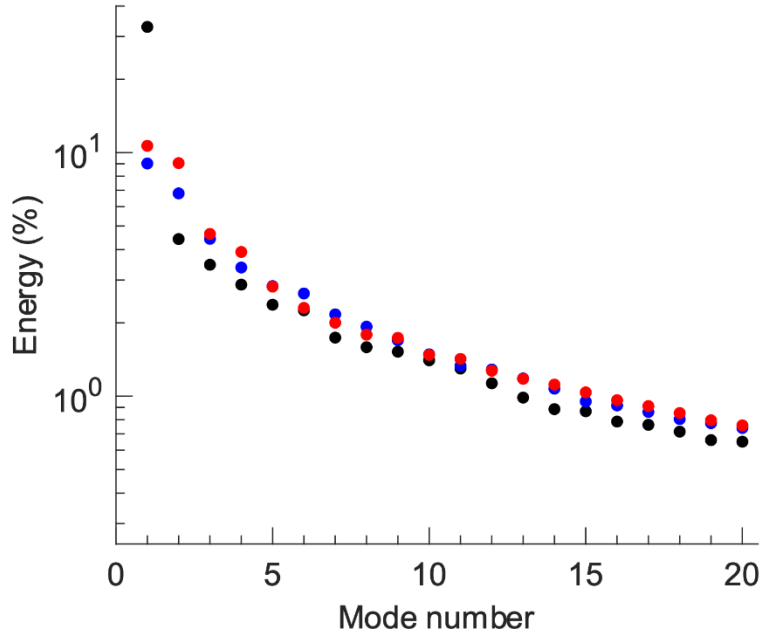
Figure 10: The distribution of POD mode energy for yaw angles $\beta = 0°$ (black), $\beta = 5°$ (blue), and $\beta = 10°$ (red).

The spatial distribution of the first four modes for the zero-yaw case are presented in Figure 11. Slices across the *y-z* plane with the respective mode magnitudes are also shown along with in-plane streamlines at *x/H*=1.5. This plane location is consistent with the measurements and subsequent POD analysis of Pavia et al. (2018). Mode one consists of two symmetric structures situated on spanwise sides. This observed pattern agrees with the first POD mode identified by Pavia et al. (2018), which they named the lateral symmetry-breaking mode. The streamline patterns also closely match those of the first mode identified by Pavia et al. (2018). Pavia et al. (2018) suggested that this lateral spatial distribution is attributable to both the bi-stability phenomenon and spanwise oscillations of the wake. This conclusion is further supported by the disproportionately high energy content of the first mode in Figure 10(a) since both of these features are characterized by strong spanwise asymmetry within the wake. The second mode consists of three lobes, one at the mid-span on the *z/H* = 0.35 plane, and the two other lobes on the *z/H* = -0.2 plane. Given that the upper and lower lobes of this mode are out of phase and amplitude switching occurs with respect to the *z/H* = 0 plane, this mode can be attributed to wall-normal wake dynamics. This spatial distribution is consistent with low order POD modes found by Pavia et al. (2018; 2020) and Fan et al. (2020) and was originally referred to as the vertical symmetry breaking mode by Pavia et al. (2018). Again, the streamlines in Figure 11(b) match those found for the second mode in Pavia et al. (2018). Mode three consists of four lobes that form a plus pattern downstream of the rear face. The sign of the amplitude for this mode indicates a pairing between the two vertically oriented lobes and the two horizontally oriented lobes, respectively. The study by Pavia et al. (2018) found a POD mode with a similar 2D distribution which they attributed to planar symmetry

20

preservation within the wake. They found that the symmetry of the low-order representation increased when this mode was included. This theory was later reaffirmed in the POD analysis of Pavia et al. (2020). The streamlines show two large recirculating regions located near the bottom of the wake. The recirculating regions at the top that were identified in Pavia et al. (2018) are however, not identified. The fourth mode consists of several smaller structures with little symmetry across any plane signifying that it is related to small-scale structures. The energy of this mode is approximately 3%. The streamline patterns for this mode primarily have wall-normal orientations.
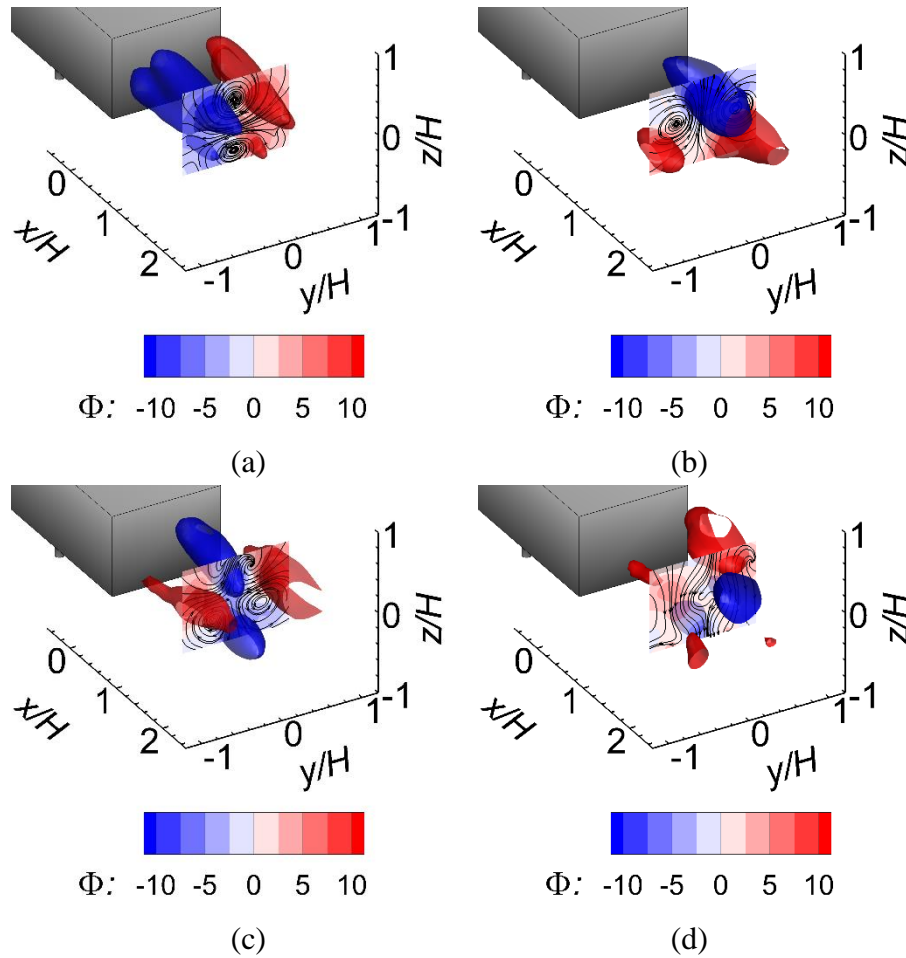

Figure 11: The spatial distribution of (a) mode 1, (b) mode 2, (c) mode 3, and (d) mode 4 of POD of the *u*-component of the velocity field at yaw angle of $\beta = 0°$. All isosurfaces are visualized at the same magnitude. The planes of mode magnitude for the streamwise velocity component (Φ) are also shown at $x/H = 1.5$ along with in plane streamlines.

Figure 12 shows the spatial organization of the first two modes for $\beta = 5°$ (a-b) and $\beta = 10°$ (c-d). Only the first two spatial modes are presented for each case as the higher order modes contain less energy. Further justification for only showing the first two spatial modes will be given in the

PSD analysis of mode coefficients at the end of this section. The spatial structures of the first and second modes for both yaw cases are very similar and therefore will be described with reference to both yaw cases. Mode one consists of a large structure favoring the upper half of the windward shear layer and two smaller structures with the opposite amplitude, positioned below the primary structure. Mode two consists of two structures also situated along the windward side of the wake. The larger structure has a downward tilt and the second structure is located above the larger primary structure. The spatial organization of these modes is associated with the turbulent motions in the windward shear layer. Lack of any structure in the leeward side also indicates the greater turbulent kinetic energy of the windward shear layer. The similarity between the mode structures for both yaw cases imply that there are no fundamental changes in the large-scale flow structure. These two leading POD modes for $\beta = 5°$ and $10°$ do not show any evidence of the symmetry–breaking mode, or the spanwise oscillations originating from the interaction of leeward and windward shear layers.
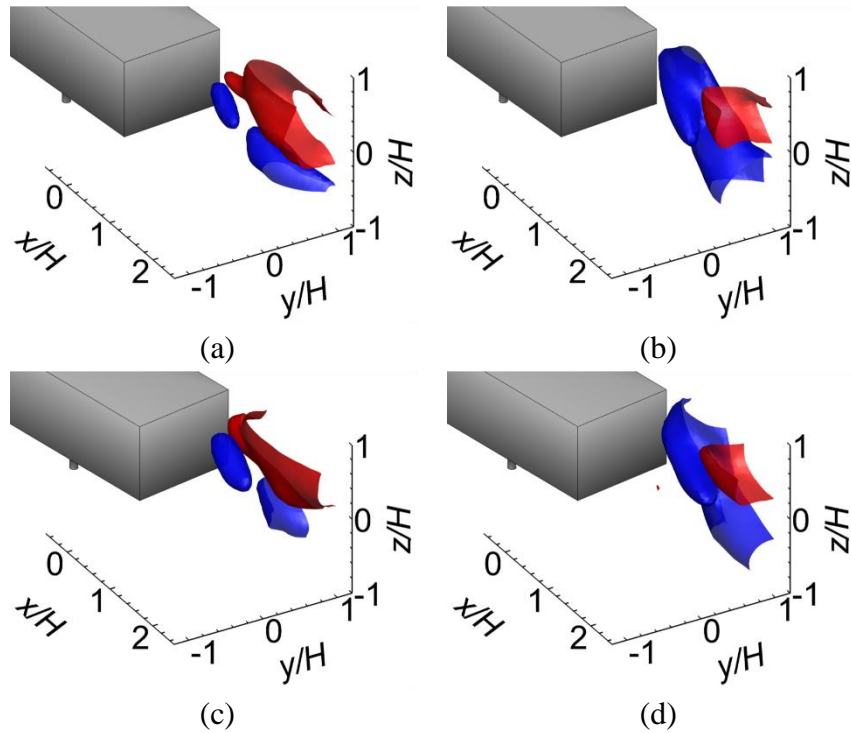

(a)   (b)

(c)   (d)

Figure 12: The spatial distribution of (a) mode 1 and (b) mode 2 for the $\beta = 5°$ case, and (c) mode 1 and (d) mode 2 for the $\beta = 10°$ case resulting from POD of the 3D velocity fields. All isosurfaces are visualized at the same magnitude.

Figure 13 shows the frequency-multiplied PSD of the time-dependent mode amplitudes. Mode one of the zero-yaw case in Figure 13(a) has high energy within low frequencies of $St_H <$ 0.1. This low frequency energy distribution is consistent with the spanwise bi-stable switching that occurs at timescales much larger than that of the shedding process. The energy distribution across

22

the low frequencies is also relatively broad which agrees with the non-periodic nature of the bi-stability phenomenon (Grandemange et al. 2013b). The first mode also contains a peak at $St_H = 0.13$ which coincides with the spanwise shedding frequency that was discussed in Section 5. The second mode peaks at $St_H = 0.19$ which matches the wall-normal shedding frequency discussed in Section 5, consistent with the spatial mode shown in Figure 11(b). A peak at $St_H = 0.19$ is also identified in modes 3 and 4 as well.

In Figure 13(b), the first and second modes for the $\beta = 5°$ case both have large peaks at $St_H = 0.19$. The first two modes of $\beta = 10°$ case in Figure 13(c), have a high energy at approximately $St_H = 0.13$ that extends to slightly higher frequencies. The mode energy at St_H smaller than 0.1 is negligible for both $\beta = 5°$ and $10°$, further indicating the lack of the bi-stable switching. A significant increase in energy is also seen when comparing the first two modes of the yawed spectra to that of the zero-yaw spectra. This is consistent with the trend identified in the PSD plots of Section 5. Modes three and four for the yawed flow cases contain no distinguishable peaks and have very low energy content throughout the spectra when compared to the first two modes.
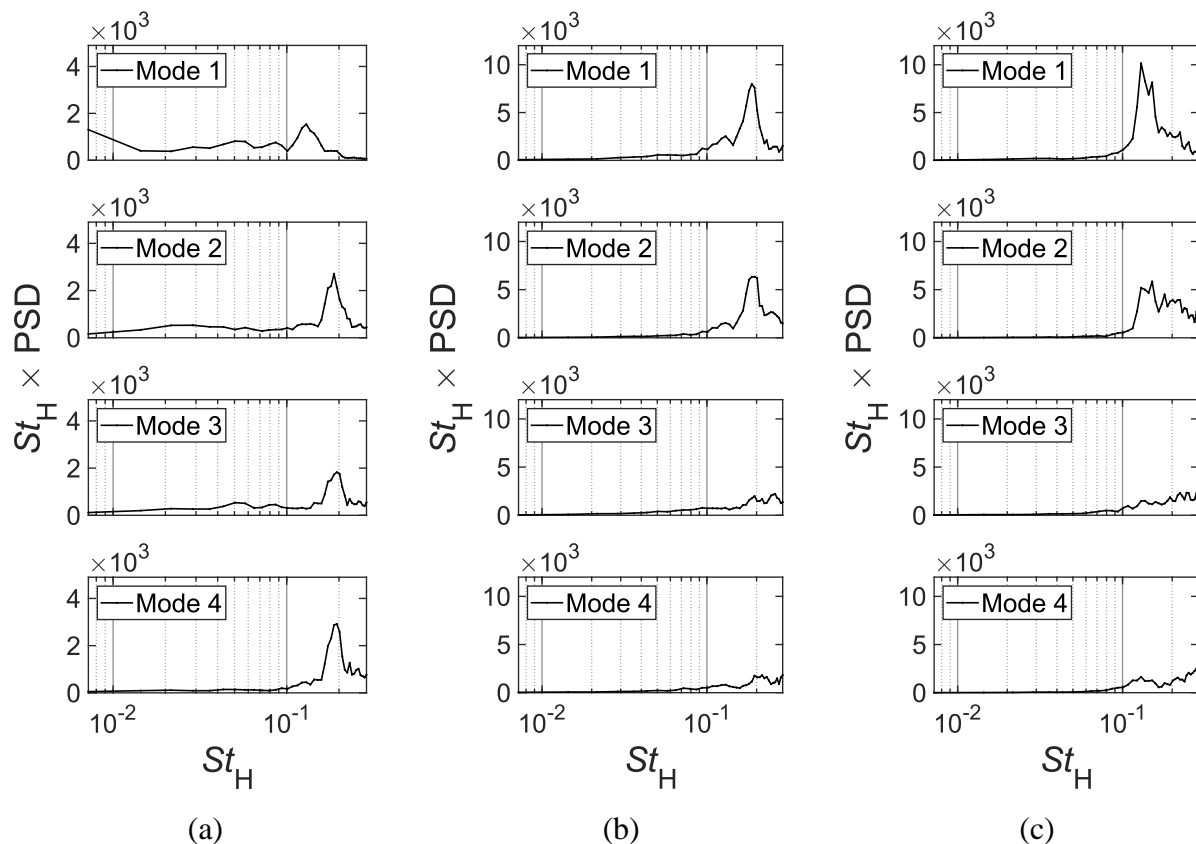

Figure 13: Frequency-multiplied PSD of the POD mode coefficients for the first four spatial modes of yaw cases (a) $\beta = 0°$, (b) $\beta = 5°$, and (c) $\beta = 10°$.

7   Conclusions

The 3D flow structures in the near-wake of a square-back Ahmed body at two yaw angles of $\beta = 5°$ and $10°$ were characterized and compared with the flow structures at $\beta = 0$. The experiments were carried out using a half-scale Ahmed body in a wind tunnel at Reynolds number of 9.2×10^4. State-of-the-art volumetric measurements of the wake flow were obtained using a large-scale time-resolved 3D-PTV that employed helium-filled soap bubbles.

The crossflow greatly increased the asymmetry of the mean flow: the separation bubble became smaller and inclined to the windward side, and a larger recirculating vortex formed on the leeward side. With increasing yaw angle, the downwash motion from the top-edge and the spanwise motion from the leeward edge of rear-face strengthened. Visualization of the vortex filaments in the mean flow showed a symmetric vortex ring for the zero-yaw case which became increasingly skewed with increasing yaw angle. The leeward portion of the vortex ring was positioned closer to the back face of the Ahmed body for the yawed cases and its windward section became weaker. Streamwise vortex filaments also appeared in the yawed wakes, primarily being located on the windward periphery of the ring vortex. The results also showed that streamwise and streamwise-spanwise Reynolds stresses became stronger and covered a larger region along the windward side as the yaw angle increased.

Spectral analysis of the wake motions in the upper-portion of the windward shear layer found three trends as yaw angle increased. The first was that the Strouhal numbers of the spectral peaks associated with the spanwise and wall-normal oscillations of the shear layer were approximately constant, and equal to 0.12-0.14 and 0.17-0.19, respectively. The second pattern was an increase in the peak magnitudes which indicated that the energy of the flow oscillations increased with the yaw angle. The last trend showed an increase of the spanwise shedding energy relative to the wall-normal shedding energy as yaw angle increased.

Proper orthogonal decomposition of the velocity field showed that the first mode of the zero-yaw case was attributed to both the bi-stability phenomenon and spanwise oscillations within the wake, while the second mode was attributed to wall-normal oscillations. When the yaw angle was increased to 5° or 10°, a more than 20% decrease in the energy of the first spatial mode relative to subsequent modes was observed. This reduction was attributed to the disappearance of the bi-stability. The first two spatial modes for the yawed cases matched closely and showed that the majority of turbulent kinetic energy within the yawed wakes were within the windward shear layer.

8   References

Ahmed SR, Ramm G, Faltin G (1984) Some salient features of the time-averaged ground vehicle wake. SAE technical paper 840300. https://doi.org/10.4271/840300

Bonnavion G, Cadot O (2018) Unstable wake dynamics of rectangular flat-backed bluff bodies with inclination and ground proximity. J Fluid Mech 854: 196–232. https://doi.org/10.1017/jfm.2018.630

Dalessio L, Duncan B, Chang C, Gargoloff JI, Tate E (2017) Accurate fuel economy prediction via a realistic wind averaged drag coefficient. SAE Int J Passeng Cars - Mech Syst 10 (1). https://doi.org/10.4271/2017-01-1535

Dalla Longa L, Evstafyeva O, Morgans AS (2019) Simulations of the bi-modal wake past three-dimensional blunt bluff bodies. J Fluid Mech 866: 791–809. https://doi.org/10.1017/jfm.2019.92

Duell EG, George AR (1999) Experimental study of a ground vehicle body unsteady near wake. SAE Technical Paper. https://doi.org/10.4271/1999-01-0812

Ebrahimian M, Sean Sanders R, Ghaemi S (2019) Dynamics and Wall Collision of Inertial Particles in a Solid-Liquid Turbulent Channel Flow. J Fluid Mech 881: 872–905. https://doi.org/10.1017/jfm.2019.749.

Evrard A, Cadot O, Herbert V, Ricot D, Vigneron R, Délery J (2016) Fluid force and symmetry breaking modes of a 3D bluff body with a base cavity. J Fluid Struct 61: 99–114. https://doi.org/10.1016/j.jfluidstructs.2015.12.001

Faleiros DE, Tuinstra M, Sciacchitano A, Scarano F (2018) Helium-filled soap bubbles tracing fidelity in wall-bounded turbulence. Exp Fluid 59: 56. https://doi.org/10.1007/s00348-018-2502-7

Faleiros DE, Tuinstra M, Sciacchitano A, Scarano F (2019) Generation and control of helium-filled soap bubbles for PIV. Exp Fluid 60: 40. https://doi.org/10.1007/s00348-019-2687-4

Fan Y, Xia C, Chu S, Yang Z, Cadot O (2020) Experimental and numerical analysis of the bi-stable turbulent wake of a rectangular flat-backed bluff body. Phys Fluid 32 (10): 105111. https://doi.org/10.1063/5.0019794

Gibeau B, Ghaemi S (2018) A modular, 3D-printed helium-filled soap bubble generator for large-scale volumetric flow measurements. Exp Fluid 59 (12): 178. https://doi.org/10.1007/s00348-018-2634-9

Gibeau B, Gingras D, Ghaemi S (2020) Evaluation of a full-scale helium-filled soap bubble generator. Exp Fluid 61 (2): 28. https://doi.org/10.1007/s00348-019-2853-8

Gohlke M, Beaudoin JF, Amielh M, Anselmet F (2007) Experimental analysis of flow structures and forces on a 3D-bluff-body in constant cross-wind. Exp Fluid 43 (4): 579–594. https://doi.org/10.1007/s00348-007-0341-z

Gohlke M, Beaudoin JF, Amielh M, Anselmet F (2008) Thorough analysis of vortical structures in the flow around a yawed bluff body. J Turbul 9: 1-28. https://doi.org/10.1080/14685240802010657

Grandemange M, Cadot O, Courbois A, Herbert V, Ricot D, Ruiz T, Vigneron R (2015) A study of wake effects on the drag of the Ahmed's squareback model at the industrial scale. J Wind Eng Ind Aerodyn 145: 282–291. https://doi.org/10.1016/j.jweia.2015.03.004

Grandemange, M, M Gohlke, and O Cadot. (2013a) Bi-Stability in the Turbulent Wake Past Parallelepiped Bodies with Various Aspect Ratios and Wall Effects. Phys Fluid 25 (9). https://doi.org/10.1063/1.4820372

Grandemange M, Gohlke M, Cadot O (2013b) Turbulent wake past a three-dimensional blunt body. Part 1. Global modes and bi-stability. J Fluid Mech 722: 51–84. https://doi.org/10.1017/jfm.2013.83

Howell J (2015) Aerodynamic drag of passenger cars at yaw. SAE Int J Passeng Cars - Mech Syst 8 (1). https://doi.org/10.4271/2015-01-1559

Khalighi B, Chen KH, Iaccarino G (2012) Unsteady aerodynamic flow investigation around a simplified square-back road vehicle with drag reduction devices. J Fluid Eng 134 (6): 061101. https://doi.org/10.1115/1.4006643

Khalighi B, Zhang S, Koromilas C, Balkanyi SR, Bernal LP, Iaccarino G, Moin P (2001) Experimental and computational study of unsteady wake flow behind a bluff body with a drag reduction device. SAE Technical Paper. https://doi.org/10.4271/2001-01-1042

Krajnović S, Davidson L (2003) Numerical study of the flow around a bus-shaped body. J Fluid Eng 125 (3): 500–509. https://doi.org/10.1115/1.1567305

Li R, Borée J, Noack BR, Cordier L, Harambat F (2019) Drag reduction mechanisms of a car model at moderate yaw by bi-frequency forcing. Phys Rev Fluid 4 (3): 034604. https://doi.org/10.1103/PhysRevFluids.4.034604

Lorite-Díez M, Jiménez-González JI, Pastur L, Cadot O, and Martínez-Bazán C (2020) Drag Reduction on a Three-Dimensional Blunt Body with Different Rear Cavities under Cross-Wind Conditions. J Wind Eng Ind Aerodyn, 200.

Lucas JM, Cadot O, Herbert V, Parpais S, Délery J (2017) A numerical investigation of the asymmetric wake mode of a squareback Ahmed body - effect of a base cavity. J Fluid Mech 831: 675–697. https://doi.org/10.1017/jfm.2017.654

Östh J, Krajnović S (2012) The flow around a simplified tractor-trailer model studied by large eddy simulation. J Wind Eng Ind Aerodyn 102: 36–47. https://doi.org/10.1016/j.jweia.2011.12.007

Östh J, Noack BR, Krajnović S, Barros D, Borée J (2014) On the need for a nonlinear subscale turbulence term in POD models as exemplified for a high-Reynolds-number flow over an Ahmed body. J Fluid Mech 747 (3): 518–544. https://doi.org/10.1017/jfm.2014.168

Pavia G, Passmore M, Sardu C (2018) Evolution of the bi-stable wake of a square-back automotive shape. Exp Fluid 59 (1): 20. https://doi.org/10.1007/s00348-017-2473-0

Pavia G, Passmore M, Varney M, Hodgson G (2020) Salient three-dimensional features of the turbulent wake of a simplified square-back vehicle. J Fluid Mech 888: A33. https://doi.org/10.1017/jfm.2020.71

Perry A-K, Pavia G, Passmore M (2016) Influence of short rear end tapers on the wake of a simplified square-back vehicle: wake topology and rear drag. Exp Fluid 57 (11): 169. https://doi.org/10.1007/s00348-016-2260-3

Rouméas M, Gilliéron P, Kourta A (2009) Analysis and control of the near-wake flow over a square-back geometry. Comput Fluid 38 (1): 60–70. https://doi: 10.1016/j.compfluid.2008.01.009

Rowin WA, Ghaemi S (2019) Streamwise and Spanwise Slip over a Superhydrophobic Surface. J Fluid Mech 870: 1127–57. https://doi.org/10.1017/jfm.2019.225

SAE International (2012) SAE wind tunnel test procedure for trucks and buses. J1252

Scarano F, Ghaemi S, Caridi GCA, Bosbach G, Dierksheide U, Sciacchitano A (2015) On the use of helium-filled soap bubbles for large-scale tomographic PIV in wind tunnel experiments. Exp Fluid 56:42. https://doi.org/10.1007/s00348-015-1909-7

Schanz D, Gesemann S, Schröder A (2016) Shake-The-Box: Lagrangian particle tracking at high particle image densities. Exp Fluid 57 (5): 70. https://doi.org/10.1007/s00348-016-2157-1

Schanz D, Gesemann S, Schröder A, Wieneke B, Novara M (2013) Non-uniform optical transfer functions in particle imaging: calibration and application to tomographic reconstruction. Meas Sci Tech 24 (2): 024009. https://doi.org/10.1088/0957-0233/24/2/024009

Sirovich L (1987) Turbulence and the dynamics of coherent structures. Part I: coherent structures. Q Appl Math 45 (3): 561–571. http://www.jstor.org/stable/43637457

Sujudi D, Haimes R (1995) Identification of swirling flow in 3-D vector fields. AIAA Paper 95-1715. https://doi.org/10.2514/6.1995-1715

Volpe R, Devinant P, Kourta A (2015) Experimental characterization of the unsteady natural wake of the full-scale square back Ahmed body: flow bi-stability and spectral analysis. Exp Fluid 56 (5): 99. https://doi.org/10.1007/s00348-015-1972-0

Volpe R, Valérie F, Arthur DS, Luis LM (2014) Forces and flow structures evolution on a car body in a sudden crosswind. J Wind Eng Ind Aerodyn 128: 114–25. https://doi.org/10.1016/j.jweia.2014.03.006

Wieneke B (2008) Volume self-calibration for 3D particle image velocimetry. Exp Fluid 45 (4): 549–556. https://doi.org/10.1007/s00348-008-0521-5

Zhu HY, Wang CY, Wang HP, Wang JJ (2017) Tomographic PIV investigation on 3D wake structures for flow over a wall-mounted short cylinder. J Fluid Mech 831: 743–778. https://doi.org/10.1017/jfm.2017.647